Quantitative Flaw Reconstruction from Ultrasonic Surface Wavefields Measured by Electronic Speckle Pattern Interferometry

T. Douglas Mast, *Member, IEEE*, and Grant A. Gordon

***Abstract*—A new method for imaging flaws in plate and shell structures is presented. The method employs two-dimensional ultrasonic surface wave data obtained by optical electronic speckle pattern interferometry (ESPI) techniques. In the imaging method, the measured out-of-plane displacement field associated with an externally excited ultrasonic Lamb wave is processed to obtain the spatial frequency domain spectrum of the wavefield. A free space Green's function is then deconvolved from the wavefield to obtain quantitative images of effective scattering sources. Because the strength of these effective sources is directly dependent on local variations in sample thickness and material properties, these images provide a direct map of internal inhomogeneities. Simulation results show that the method accurately images flaws for a wide range of sizes and material contrast ratios. These results also demonstrate that flaw features much smaller than an acoustic wavelength can be imaged, consistent with the theoretical capability of the imaging method to employ scattered evanescent waves. Reconstructions are also obtained from ultrasonic Lamb wave displacement fields recorded by ESPI in a flawed aluminum plate. These reconstructions indicate that the present method has potential for imaging flaws in complex structures for which ESPI wavefield measurements cannot be straightforwardly interpreted.**

I. Introduction

A major problem in nondestructive evaluation is the early detection of structural damage in vehicles and other critical machinery. For example, concern about mechanical safety in aircraft structures is growing as the median age of active commercial and military aircraft increases. Despite recent research and development activities, many in the commercial aviation community believe that few, if any, of the existing inspection requirements can be addressed by current and emerging wide area inspection systems. A major concern is early detection of widespread fatigue damage. An ideal imaging inspection system for aircraft and similar machinery would operate in real time, provide quantitative characterization of flaws in plate-like structures, allow detection of small cracks even in multilayer structures, and establish a precise and reproducible correspondence between indications and actual flaws [1].

One approach to improve flaw detection in plate-like structures is to detect defects using the scattered, reflected, and transmitted response of transient high frequency Lamb waves within the structures of interest. Such methods are based on detectable wave effects such as reflection, scattering, and mode conversion that occur when elastic waves interact with areas of inhomogeneity, such as disbonds, cracks, and delaminations. Recent experimental studies have investigated the use of Lamb wave amplitude and time-of-flight measurements as indicators of defects in lap splice joints [2]–[5]. It has also been shown that the generation and reception of ultrasonic Lamb waves on painted aluminum structures are not significantly influenced by the presence of paint in thicknesses common to the aircraft industry [6]. In addition, others have investigated the use of Rayleigh-Lamb waves for industrial material characterization [7]–[10]. The use of ultrasonic Lamb waves appears to be a viable inspection approach for lap-splice inspection and industrial material characterization.

A more general approach to nondestructive testing using Lamb waves is Lamb wave tomography [11]–[14] in which two-dimensional Lamb wave speed attenuation maps are quantitatively reconstructed from multiple pitch-catch measurements. This technique has been used to successfully image flaws but possesses weaknesses characteristic of its algorithm. For example, multiple measurements are required to construct a data set for the inversion process, and the image resolution depends on the number of independent measurements and their orientation. Furthermore, the commonly used filtered backprojection reconstruction algorithms are limited because they neglect scattering effects and assume straight, unperturbed propagation paths for the Lamb waves. More sophisticated reconstruction algorithms (e.g., [15], [16]) can provide improved image quality at the cost of increased computational complexity; such algorithms still require many independent measurements.

For practical in situ nondestructive testing, rapid detection of ultrasonic waves by noncontacting methods is of particular interest. As discussed in various texts and review articles (e.g., [17], [18]), there exists a number of

Manuscript received August 13, 1999; accepted September 5, 2000. This research was partially supported by the Institute for Manufacturing and Sustainment Technologies at the Applied Research Laboratory of The Pennsylvania State University. The Institute is a non-profit organization sponsored by the United States Navy Manufacturing Technology (MANTECH) Program of the Office of Naval Research (contract number N00039-97-0042). Any opinions, findings, conclusions, or recommendations expressed in this material are those of the authors and do not necessarily reflect the views of the U.S. Navy.

T. D. Mast is with the Applied Research Laboratory, The Pennsylvania State University, University Park, PA 16802.

G. A. Gordon is with McDermott Technology Inc., Lynchburg Research Center, Lynchburg, VA 24506.

optical techniques for sensing small local displacements on plates and shells. Many of these techniques, when used on rough samples, focus the detection beam onto the surface because the system sensitivity is maximized when only a single speckle spot is detected [17]. (In principle, many of these techniques, including confocal Fabry-Perot and two-wave mixing photorefractive interferometry, can be extended to wide area sensing applications; however, the ESPI methods discussed subsequently have received more attention for a number of practical reasons, including simplicity of design, ease of use, and reduced recording media resolution requirements.) Recently, a number of investigators have employed scanned lasers to generate and detect ultrasound in thin structures, and have shown the feasibility of measuring thickness and elastic properties [10] and of constructing tomographic attenuation maps [12] as well as B-scan and C-scan images [19]–[21] from laser-detected ultrasound. A disadvantage common to these methods is that practical large area imaging is achieved using mechanical scanning, so that high resolution inspection of real structures can be time-consuming and mechanically complex.

In addition to optical approaches, ultrasonic Lamb waves can also be generated and detected by other noncontact techniques, such as air-coupled transducers and electromagnetic acoustic transducers (EMAT) [13], [22], [23] and combinations of these techniques with laser-based detection [24], [25]. These approaches, like point-wise optical measurements of ultrasound, require either mechanical scanning or multiple-element arrays to measure full surface wavefields.

Full-field optical detection of ultrasound is a potentially powerful method for rapid, wide area inspection of structures. Because no mechanical scanning is required, data for nondestructive evaluation can be acquired faster than by single-point interferometric methods. Techniques employed for full-field detection of acoustic waves in structures have included a heterodyned holographic system for visualizing traveling surface acoustic wavefronts [26], a pulsed holographic system for imaging laser-generated Rayleigh waves [27], and double-pulsed holographic interferometry for visualization of ultrasonic waves on surfaces eroded by particle impact [28].

An ESPI technique known as digital phase stepping shearography has also been introduced for imaging ultrasonic surface waves [29]–[31]. Shearography is distinct from holography because the object and reference beams share a common optical path. Because of this common path design, shearography has a number of advantages over holographic techniques, including tolerance to rigid body motion, reduced laser coherence requirements, compact design, and convenient sensitivity control. Recently, this technique has been used to image modes of bar vibration [29]–[31], ultrasonic waves in plates [29]–[32], and ultrasonic Lamb waves scattered by defects in aluminum plates [31] and C/epoxy plates [32].

Although full-field ESPI measurements of ultrasonic Lamb waves provide a fast, noncontact method to image traveling ultrasonic elastic waves, these methods are not directly applicable to many in situ nondestructive testing problems. In real-world structures, Lamb waves interact not only with flaws, but also with harmless inhomogeneities such as rivets, ribs, and other structural features. When inspecting a full-field ESPI image of ultrasonic wave propagation in such a structure, scattering and other wave effects caused by normal structure can be difficult to distinguish from effects caused by defects.

The present paper offers a new nondestructive testing method that can provide real-time quantitative images of plate structures without the requirement of mechanical scanning, the limiting approximations of Lamb wave tomography, or the indirectness of ultrasonic wavefield visualization. In the present study, surface wavefields measured by a common ESPI technique, TV holography, provide the input data for an inverse scattering problem whose solution is a quantitative map of the plate structure. These two-dimensional wavefields are inverted by deconvolving an appropriate Green's function from the total field, yielding high resolution, quantitative flaw images. Because of the broadband spatial frequency information contained in the full two-dimensional surface wavefield, this technique allows quantitative reconstruction of flaws from a single optically measured image of the elastic wavefield. The noncontact nature of the data collection means that images can be obtained and combined without concern for the distorting effects of coupling inconsistencies common among point scanning techniques. Furthermore, the new imaging method makes full use of all available wavefield data, including evanescent waves, strong scattering, and multiple scattering.

This new nondestructive testing method is derived subsequently. Reconstructions performed using simulated data demonstrate the potential of the method for flaw imaging with extremely high resolution. Preliminary experimental results show that the method provides accurate images of flaws in real plate structures.

II. Theory

The current imaging method provides a quantitative way to image subsurface flaws in plate-like structures using full-field surface measurements of ultrasonic Lamb wave propagation. The starting point for this method is the wavefield induced by a narrowband ultrasonic source applied to an inhomogeneous medium. For simplicity, the structure will be assumed to be sufficiently thin that a two-dimensional propagation model is appropriate.

When the structure is driven below the cutoff frequency of higher order modes, the resulting wavefield can be effectively limited to a single Lamb wave mode. In this case, the inhomogeneous plate can be characterized by a single spatially dependent wavespeed $c(\mathbf{r})$. Previous imaging studies employing time-of-flight ultrasonic tomography [11], [13], [14] confirm that the single wavespeed model can be appropriate for propagation of Lamb waves in flawed plates.

This wavespeed is directly related to parameters such as the local density, thickness, and elastic constants of the plate [33].

The Lamb wavefield is assumed to be generated by an applied ultrasonic source such as a contacting or noncontacting transducer; for such a source operating in continuous wave mode, the spatially and temporally dependent source strength can be written in the form $Q(\mathbf{r})e^{-i\omega t}$. The surface displacement $u(\mathbf{r})$ then obeys the inhomogeneous Helmholtz equation

$$\nabla^2 u(\mathbf{r}) + \frac{\omega^2}{c(\mathbf{r})^2}\, u(\mathbf{r}) = Q(\mathbf{r}) \tag{1}$$

where $\omega = 2\pi f$ is the radial frequency of the driving signal.

Eq. (1) can also be written in a form such that the displacement $u(\mathbf{r})$ depends both on the real source $Q(\mathbf{r})$ and an effective scattering source,

$$\nabla^2 u(\mathbf{r}) + k_0^2\, u(\mathbf{r}) = Q(\mathbf{r}) + q(\mathbf{r})\, u(\mathbf{r}), \tag{2}$$

where the scattering potential $q(\mathbf{r})$ is given by

$$q(\mathbf{r}) = -k_0^2 \left(\frac{c_0^2}{c(\mathbf{r})} - 1 \right) = -k_0^2\, \gamma(\mathbf{r}). \tag{3}$$

c_0 is the nominal average wavespeed of the generated Lamb wave mode in the medium, and k_0 is the wavenumber ω/c_0. The contrast function $\gamma(\mathbf{r})$ is analogous to the compressibility contrast γ_κ [34] for a fluid medium of constant density. The effective source term $q(\mathbf{r})u(\mathbf{r})$ in (2) can be regarded as the source of scattered waves; the real source term $Q(\mathbf{r})$ can be regarded as the source of the incident wave.

Transformation of (2) using Green's theorem [35] yields the integral equation

$$u(\mathbf{r}) = -\int\int \Big(Q(\mathbf{r}) + q(\mathbf{r}) u(\mathbf{r}) \Big)\, G_0(|\mathbf{r} - \mathbf{r}_0|)\, d^2 r_0, \tag{4}$$

so that the complex displacement $u(\mathbf{r})$ is given as an integral of the two-dimensional free-space Green's function $G_0(\mathbf{r}) = i/4\, H_0^{(1)}(k_0 r)$ weighted by the real and effective source terms from (2).

In most inverse scattering problems, (4) cannot be solved directly to find the scattering potential $q(\mathbf{r})$ because the wavefield $u(\mathbf{r})$ is only measured at a limited number of locations (typically at the elements of a receiving transducer). However, other measurement techniques, such as electronic speckle pattern interferometry, allow measurement of the wavefield over a large surface area. When the measurement area includes the support of the contrast function $\gamma(\mathbf{r})$, (4) can be directly inverted by the methods outlined subsequently.

Eq. (4) expresses the total displacement as a convolution of the free space Green's function with a source term that includes both the real source $Q(\mathbf{r})$ and an effective source term $q(\mathbf{r})\, u(\mathbf{r})$. In real space and wave space, respectively, this convolution can be written

$$\begin{aligned} u(\mathbf{r}) &= -[Q(\mathbf{r}) + q(\mathbf{r})\, u(\mathbf{r})] \otimes G_0(\mathbf{r}) \\ \hat{u}(\mathbf{k}) &= -\mathbf{F}[Q(\mathbf{r}) + q(\mathbf{r})\, u(\mathbf{r})] \hat{G}_0(\mathbf{k}) \end{aligned} \tag{5}$$

where $\mathbf{F}$ and the hat accent represent the two-dimensional spatial Fourier transform given by

$$\hat{\psi}(\mathbf{k}) = \mathbf{F}[\psi(\mathbf{r})] = \frac{1}{2\pi} \int\int \psi(x, y)\, e^{i(k_x x + k_y y)}\, dx\, dy. \tag{6}$$

The source terms can be extracted from the total wavefield by the deconvolution operation [36]

$$Q(\mathbf{r}) + q(\mathbf{r})\, u(\mathbf{r}) = -\mathbf{F}^{-1} \left[\frac{\hat{u}(\mathbf{k})}{\hat{G}_0(\mathbf{k})} \right] \tag{7}$$

where $\mathbf{F}^{-1}$ represents the inverse two-dimensional spatial Fourier transform

$$\psi(\mathbf{r}) = \mathbf{F}^{-1}[\hat{\psi}(\mathbf{k})] = \frac{1}{2\pi} \int\int \hat{\psi}(k_x, k_y)\, e^{-i(k_x x + k_y y)}\, dx\, dy. \tag{8}$$

Eq. (7) can be implemented using discrete Fourier transformation. If the wavefield is sampled over a region of interest where no real sources exist [i.e., outside the support of $Q(\mathbf{r})$], a discrete implementation of (7) yields a quantitative reconstruction of the effective scattering sources within the region of interest. With incorporation of a lowpass spatial frequency filter to ensure stability of inversion, the discrete implementation of (7) can be rewritten to yield an estimate for the wavespeed contrast function $\gamma(\mathbf{r})$,

$$\tilde{\gamma}(\mathbf{r}) = \mathbf{FFT}^{-1} \left[\frac{\hat{u}(\mathbf{k})\ \phi(\mathbf{k})}{\hat{G}_0(\mathbf{k}) + \epsilon\ \|\hat{G}_0\|} \right] \Big/ \left[k_0^2\, u(\mathbf{r}) \right] \ , \tag{9}$$

where $\tilde{\gamma}(\mathbf{r})$ represents an estimation of the actual contrast function $\gamma(\mathbf{r})$, $\mathbf{FFT}$ represents a fast Fourier transform implementation of the discrete Fourier transform, $\phi(\mathbf{k})$ is a lowpass filter that removes spatial frequencies for which the denominator of (7) is small, and a small parameter ϵ is multiplied by the L^2 norm of $\hat{G}_0(\mathbf{k})$ in the denominator. The parameter ϵ is analogous to a regularization parameter but is needed here only because $\hat{G}_0(\mathbf{k})$ can become vanishingly small (to within numerical precision) for $|\mathbf{k}| \gg k_0$. Very small values of ϵ (e.g., near the precision limit of the numerical computation) provide sufficient correction for this numerical problem.

In practical measurements, uncertainties in the estimated total field $u(\mathbf{r})$ can cause problems with numerical implementation of (9). At locations where the complex wavefield $u(\mathbf{r})$ is near zero, this uncertainty can result in large errors in the estimated contrast function $\tilde{\gamma}(\mathbf{r})$. This difficulty can be overcome by employing an approximate form of (9), in which the total wavefield is replaced by a function with unchanged phase but with unit magnitude. (Because the total measured wavefield can be normalized

to have a mean amplitude of unity, this approximation does not significantly compromise the quantitative accuracy of the present reconstruction method.) Under this approximation, (9) takes the form

$$\tilde{\gamma}(\mathbf{r}) \approx \mathbf{FFT}^{-1}\left[\frac{\hat{u}(\mathbf{k})\ \phi(\mathbf{k})}{\hat{G}_0(\mathbf{k}) + \epsilon\,\|\hat{G}_0\|}\right] \Big|u(\mathbf{r})\Big| \Big/ \left[k_0^2\ u(\mathbf{r})\right]. \tag{10}$$

Several details of implementation need to be considered when applying (10) to the problem of reconstructing flaws from ESPI wavefield measurements. First, a single optical wavefield measurement provides a snapshot of the wavefield at one temporal epoch. Such a measurement is equivalent to measurement of the real part of $u(\mathbf{r})$ for single frequency data. An estimated complex wavefield, required for inversion according to (10), is obtained by applying Hilbert transformation along the principal direction of propagation. For example, if the propagation direction of the incident wave is ξ and the measured real field is $u_r(\mathbf{r})$, the total field can be approximated as

$$u(\mathbf{r}) = u_r(\mathbf{r}) + i\,\mathbf{H}_\xi[u_r(\mathbf{r})] \tag{11}$$

where $\mathbf{H}_\xi$ represents the one-dimensional Hilbert transform applied along the ξ-direction. Eq. (11) is exact for plane waves propagating only in the ξ direction but is only approximately correct in the presence of scattering.

Another detail of implementation involves the choice of appropriate representations for the free space Green's function $G_0(\mathbf{r})$ and its spatial Fourier transform $\hat{G}_0(\mathbf{k})$. Although $\hat{G}_0(\mathbf{k})$ can be evaluated analytically, use of this analytic transform can lead to incorrect approximation of discrete convolutions similar to (5) [37], [38] as well as corresponding errors in the deconvolution represented by (10). That is, the exact form of $\hat{G}_0(\mathbf{k})$ corresponds to a Green's function of infinite extent in real space, and discrete Fourier representation implicitly assumes spatial periodicity of the effective sources from (5). Thus, implementation of (10) using discrete Fourier transformation and an exact expression for $\hat{G}_0(\mathbf{k})$ would result in deconvolution of the Green's function from a wavefield containing fictitious image sources as well as the true effective sources. This "wraparound" problem is avoided here, in a manner similar to that described in [39], by use of a Green's function windowed to have the same spatial extent as the wavefield sampled for inversions. Further discussion of these errors, in the context of acoustic field computations using the angular spectrum method, is given in [37] and [40].

In the reconstructions reported here, spatial domain sampling and shading of the Green's function was performed on a uniform grid symmetrically oriented about the origin such that the origin ($|\mathbf{k}| = 0$) occurred midway between grid points in both the k_x and the k_y directions. Thus, the smallest spatial frequency magnitudes sampled were $|\mathbf{k}| = (\sqrt{2}/2)\Delta k$, where Δk is the spatial frequency step size. Symmetric sampling of the Green's function can result in greater numerical accuracy [40], and numerical difficulty associated with the singularity of $G_0(\mathbf{r})$ at the origin is avoided by the grid scheme chosen.

III. Simulations

The method described previously has been tested using simulated displacement wavefield data for inhomogeneous two-dimensional media. One simulation employed an exact solution for scattering from a circular flaw of constant wavespeed [34]; this flaw could correspond, for instance, to a localized thickness variation in a thin plate of homogeneous material properties. The incident wavefield was defined as the unit amplitude plane wave $e^{ik_0 x}$. Wavefields computed for circles of given radii and wavespeeds were employed in (10) to image the flaw contrast. In the circle simulations, the real parts of computed wavefields were computed on a square 256×256 grid with width dimensions equal to $4a$, where a is the radius of the circle. The complex wavefield was determined by Hilbert transformation along the direction of propagation for the incident wave. Free space Green's functions were computed on the same grid using the wavenumber of the incident field. Before Fourier transformation was applied, both the wavefield and the Green's function were windowed by a two-dimensional cosine-taper function defined by the Blackman window

$$W(r) = \begin{cases} 0.42 + 0.5\cos\frac{\pi r}{4a} + 0.08\cos\frac{\pi r}{2a}, & r < 4a \\ 0, \quad r > 4a, \end{cases} \tag{12}$$

where the window argument is the radius $r = |\mathbf{r}| = \sqrt{x^2 + y^2}$. In implementation of (10) for image reconstruction, a spatial frequency Blackman window,

$$\phi(\mathbf{k}) = \begin{cases} 0.42 + 0.5\cos\frac{\pi k}{k_{\max}} + 0.08\cos\frac{\pi k}{k_{\max}}, & k < k_{\max}, \\ 0, \quad k > k_{\max}, \end{cases} \tag{13}$$

was employed.

For the reconstructions of circular flaws, the spatial frequency cutoff employed was $k = \pi/\Delta x$, where Δx was the spatial step. The parameter ϵ was set to 10^{-8}. Fig. 1 shows the computed (real) displacement fields used for reconstruction. The examples cover a multiplicative range of eight in both the contrast $\gamma = c_0^2/c^2 - 1$ and the normalized wavenumber $k_0 a$. For the smallest wavenumber employed, the circular flaw spans less than a wavelength in diameter; for the largest wavenumber, the flaw spans about six wavelengths. The range of contrast investigated is $0.1 < \gamma < 0.8$. For the range of these two parameters employed, the scattered field exhibits phenomena ranging from weak scattering to strong focusing effects.

Reconstructed contrast functions $\tilde{\gamma}(\mathbf{r})$, obtained by applying (10) to the computed fields of Fig. 1, are shown in Fig. 2 for the simulation employing a circular flaw. To show detail, the reconstructions are presented for square regions with dimensions one-half of those of Fig. 2. The circle is observed to be well resolved throughout the parametric range employed. For the lowest wavenumber employed ($k_0 a = 2.5$), the circle's edges are clearly resolved on scales much less than the wavelength. This result shows the capability of the reconstruction method to achieve resolution

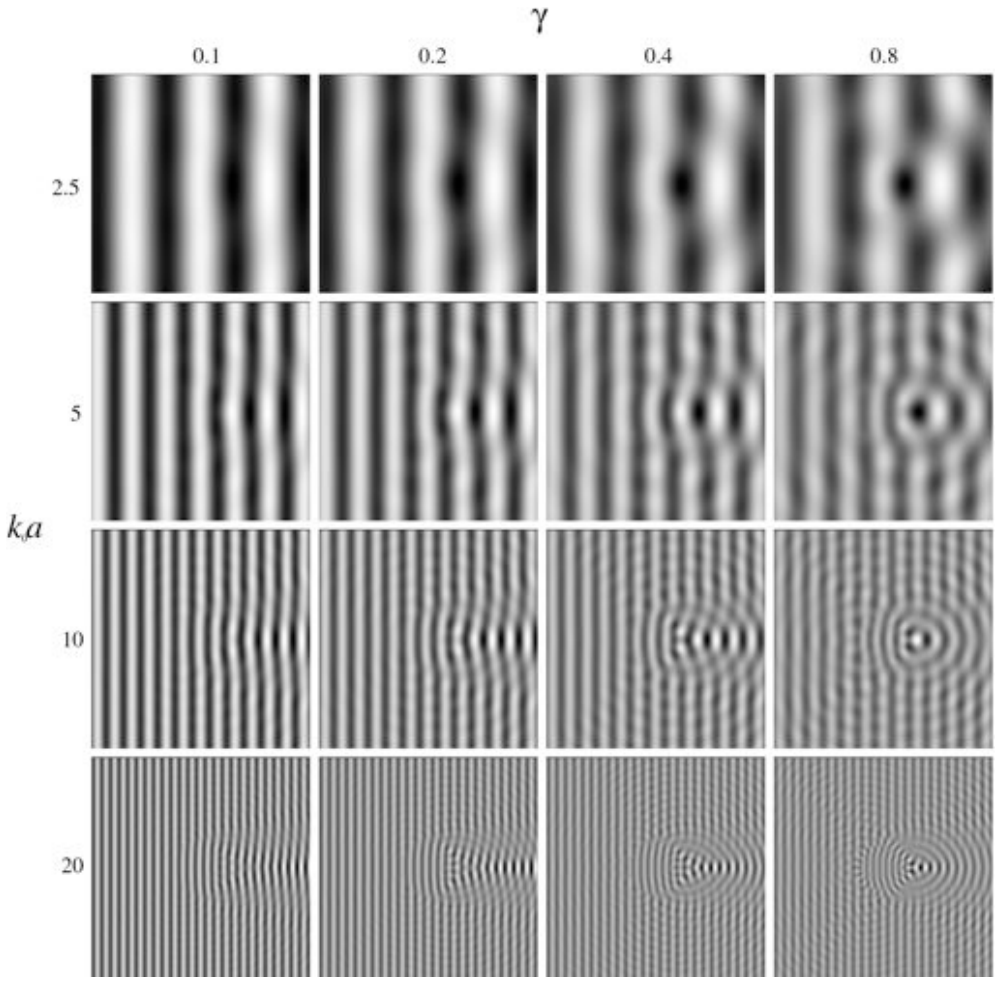

Fig. 1. Computed real wave fields for a circular flaw with contrast varying between 0.1 and 0.8 for wavenumbers such that $2.5 < k_0 a < 20$. Each plot shows a square region of dimensions $8a$ on each side. Wavefields are shown on a bipolar linear grayscale; white indicates maximum positive amplitude, and black represents maximum negative amplitude.

beyond the usual diffraction limit. For linearized inverse scattering methods employing far-field scattering data, the maximum reconstructed spatial frequency is k_0/π, which corresponds to a spatial feature size of one-half wavelength [41]. Thus, to reconstruct features on scales smaller than one-half wavelength, the present method exploits non-propagating (i.e., evanescent) components of the displacement wavefield. The reconstruction method is also observed to be valid for large (compared with the ultrasonic wavelength) flaws and strong scattering, because the circle is well reconstructed even for the smallest wavelengths and largest contrasts employed.

For comparison, reconstructions of the same circular flaws were performed using a diffraction tomography method, based on retransmitted eigenfunctions of the far field scattering operator, presented in [16]. These reconstructions employed the weak scattering form of the eigenfunction method, which is equivalent to standard filtered backpropagation [42] but can provide more efficient reconstructions [43]. The synthetic data set for each reconstruction was the complex scattered displacement on a measurement circle of radius 200 mm for 128 incident wave directions and 128 measurement directions. Fig. 3 shows the real part of each reconstruction in a format analogous to that of Fig. 2. In almost all cases, the diffraction tomography reconstructions are inferior to those obtained by the present inverse scattering method. Diffraction tomography reconstructions for low wavenumbers show poor resolution because these reconstructions do not employ evanescent wave scattering information. Reconstructions for large wavenumbers and contrasts are dominated by artifacts, indicating that the weak scattering approximation is not valid for these cases. This comparison confirms that the present inverse scattering method, although employing only one optical measurement of the two-dimensional wavefield, provides flaw reconstructions superior to diffraction tomography reconstructions over a wide range of flaw contrasts and sizes.

To characterize the achievable resolution of the current reconstruction method, a second simulation was performed using a finite difference, time domain (FDTD) method that computes the total displacement wavefield for arbitrarily shaped flaws. The FDTD algorithm employed has been described elsewhere [44], [45]. In the FDTD simulation,

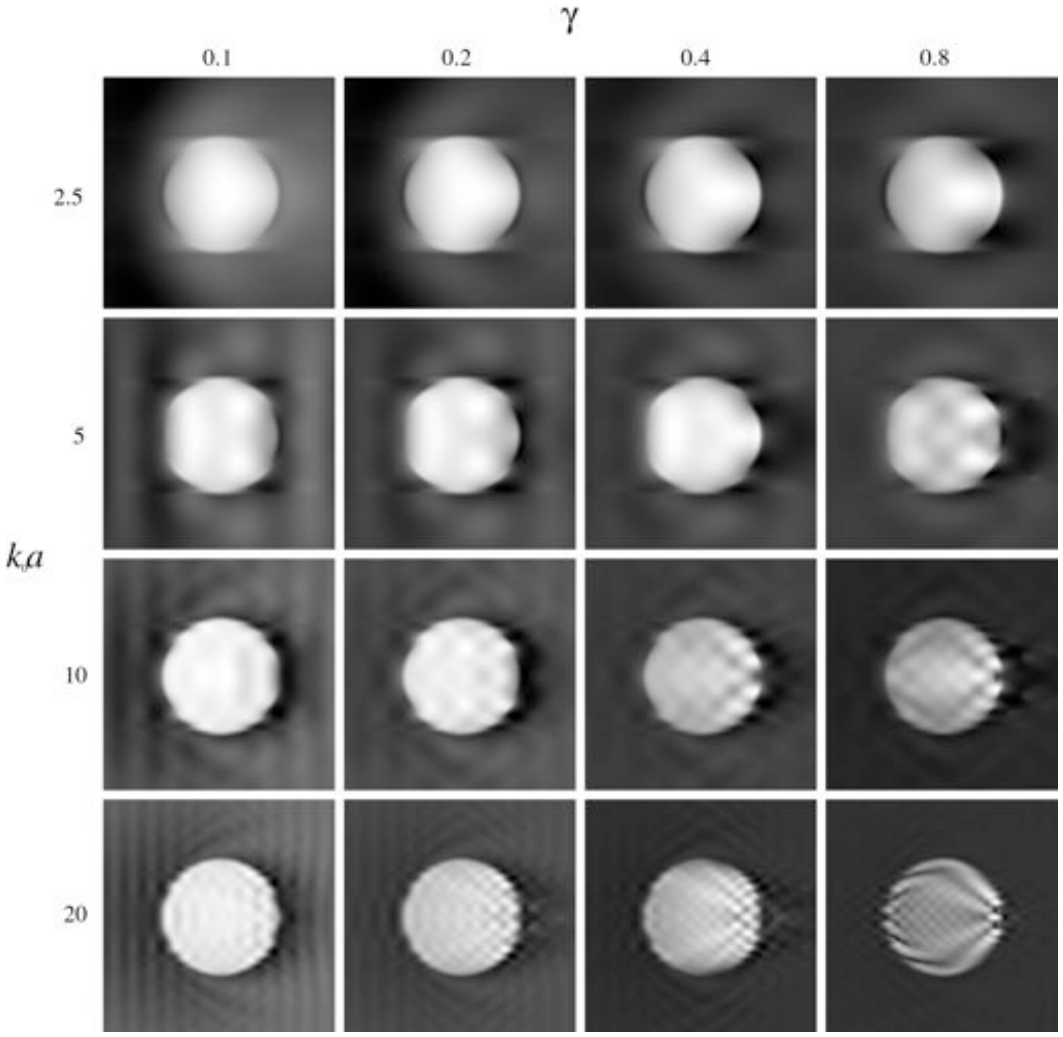

Fig. 2. Contrast functions Re$[\tilde{\gamma}(r)]$ reconstructed from the simulated ESPI data of Fig. 1 for a circular flaw with contrast varying between 0.1 and 0.8 for wavenumbers such that $2.5 < k_0a < 20$. Each plot shows a square region of dimensions $4a$ on each side. Reconstructions are shown on a bipolar linear grayscale; white indicates maximum amplitude.

a wavefield was generated by a point source realized by applying a sinusoidal variation at one grid point:

$$u(x_s, y_s, t) = A \sin(\omega t). \tag{14}$$

The total wavefield was then computed on a rectangular domain with a wavespeed $c(i, j)$ defined at each grid point. Radiation boundary conditions optimally matched to a point source in a homogeneous medium were applied at each boundary. Using an approach similar to that described in [46], it can be shown that appropriate boundary conditions for absorption of a point source at the origin are

$$\frac{\partial u}{\partial r} = \left(\cos\theta + \frac{\sin^2\theta}{\cos\theta}\right)\frac{\partial u}{\partial x}, \text{ right and left boundaries,}$$
$$\frac{\partial u}{\partial r} = \left(\sin\theta + \frac{\cos^2\theta}{\sin\theta}\right)\frac{\partial u}{\partial y}, \text{ top and bottom boundaries,} \tag{15}$$

where θ is the direction angle of a vector pointing from the origin to the local boundary point.

Finite differencing was carried out for a time period sufficient for the wavefield to approach a steady state. A displacement wavefield snapshot $u(x, y)$ was then output for a single time step. The wavefield was cropped to a square region chosen not to include the original point source. The total complex wavefield was estimated using Hilbert transformation along the principal propagation direction, as performed previously for the circle simulation. A square region of the wavefield including the flaw was then extracted from the total wavefield and was inverted by the methods described previously for the circle simulation.

The flaw employed for the finite difference simulations, a discretized Sierpinski triangle fractal sampled at thirty points per wavelength, is shown in Fig. 4 together with example wavefields and contrast reconstructions for the finite difference simulation. Each edge of the triangle spans about five wavelengths. Reconstructions are shown for maximum triangle contrasts γ of 0.2, 0.4, and 0.8. In most cases, the triangles of the second smallest scale (height less than one-sixth wavelength) appear to be clearly resolved,

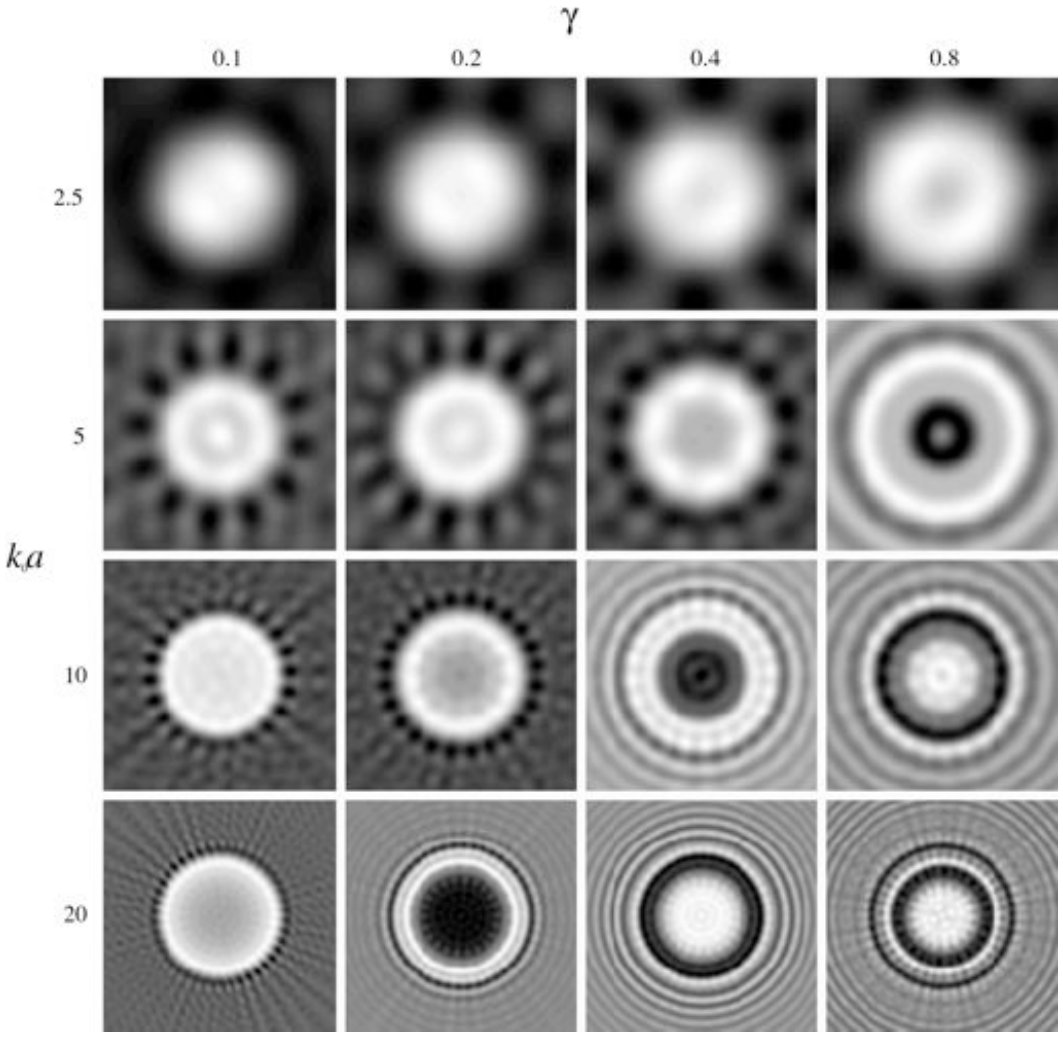

Fig. 3. Contrasts Re[$\tilde{\gamma}(r)$] reconstructed by diffraction tomography for a circular flaw with contrast varying between 0.1 and 0.8. The figure format is identical to that of Fig. 2.

suggesting (as do the circular flaw reconstructions described previously) that the image resolution is enhanced by the presence of evanescent waves.

IV. Experiments

Flaw reconstructions have been obtained from surface wavefields measured by a digital phase stepping holography technique. The modified ESPI system used to collect the digital phase-stepping holography data, described in detail in [47], is shown in Fig. 5(a). Two coherent optical wavefronts, one of which has reflected off the plate surface of interest, combine to form an interference pattern at the image plane of a Pulnix 960×680 pixel CCD camera. Interference patterns corresponding to two plate displacement states are recorded using a series of four different optical phase shifts for each displacement state. Optical path length differences corresponding to optical phase shifts of of 0, $\pi/2$, π, and $3\pi/2$ are produced by driving a PZT-stack-mounted mirror to predetermined positions. From the resulting data, the optical phase at all points in the field can be calculated for the images of both displacement states. After this processing, the composite image can achieve a displacement resolution up to 1/1000 of an optical wavelength; standard fringe pattern resolution is only one-half an optical wavelength. The signal-to-noise ratio realized by the visual contrast of the resulting phase map pattern is also increased substantially over fringe pattern techniques.

To capture traveling ultrasonic Lamb waves, the digital phase-stepping ESPI system has been combined with laser modulation. By driving an acousto-optic modulator with a pulse sequence synchronized to the ultrasonic source, the transmitted laser light stroboscopically freezes the motion of the sample at a specified ultrasonic phase. The SNR of the final difference interferogram can be optimized by ensuring that the two plate displacement states are large and opposite in direction. For traveling single frequency ultrasonic wavefields, this criterion is met when the two displacement conditions employed are separated in phase by π.

Phase stepping, real time data display, and stroboscopic illumination were coordinated by synchronizing the drive

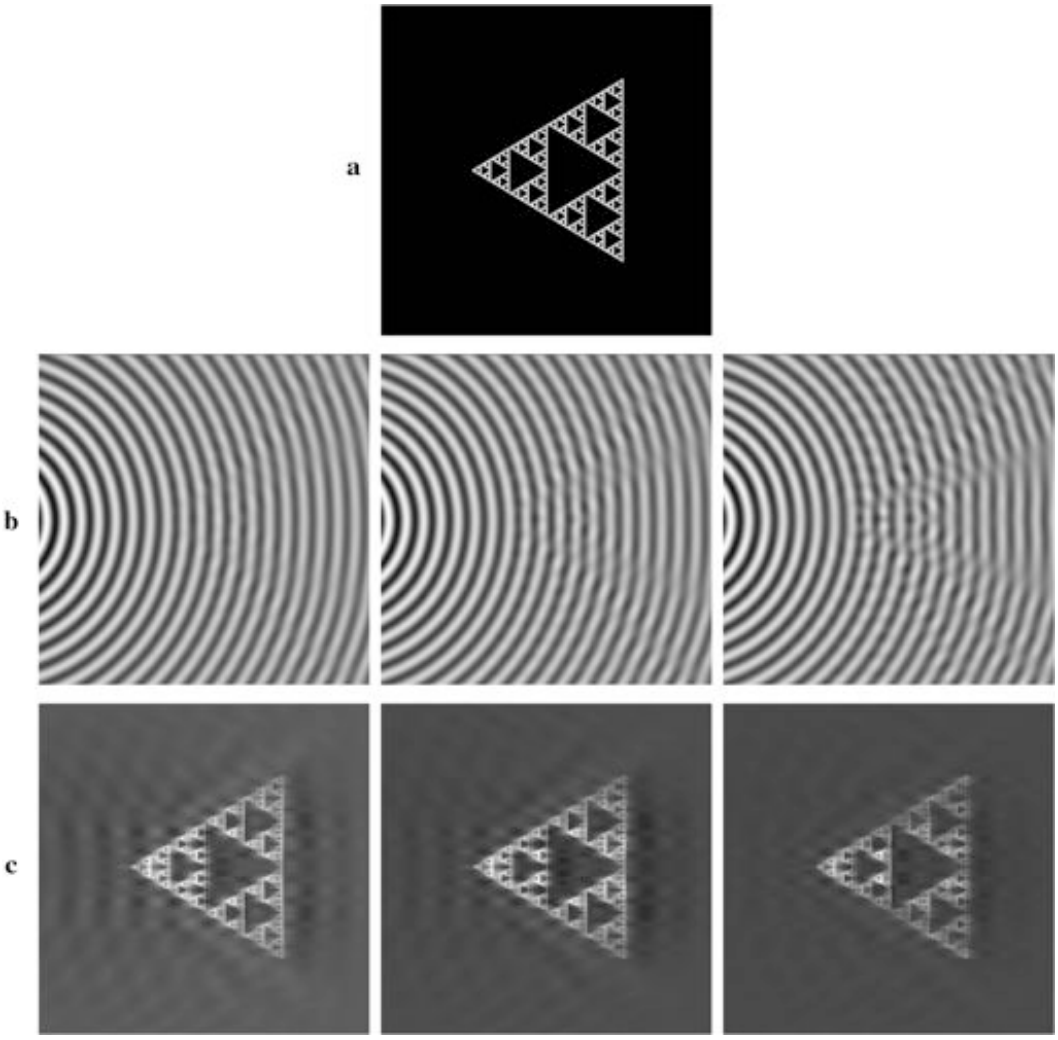

Fig. 4. Computed real wave fields and reconstructions for a fractal-shaped test object with contrasts of 0.2, 0.4, and 0.8 [left to right in panels (b) and (c)] and a wavenumber of 10 rad/mm. a) Sierpinski triangle fractal-shaped flaw. The square region shown is 5.76 mm on each side. b) Wavefield snapshots computed by the finite-difference algorithm. Each panel shows a square region of dimensions of 11.52 mm on each side. Wavefields are shown on a bipolar linear grayscale; white indicates maximum positive amplitude, and black represents maximum negative amplitude. c) Reconstructions computed using the simulated wavefield snapshots. Each panel shows a square region of dimensions 5.76 mm on each side. The real part of each flaw reconstruction is shown on a bipolar linear grayscale; white indicates maximum positive amplitude.

signal and acousto-optic modulator through a switching box controlled according to the data acquisition rates established by the computer. Fig. 5(b) shows the timing relationship among the various operations. For clarity, the drive signal and the laser modulation signal are shown at a frequency significantly lower that those used for data collection.

Large amplitude Lamb waves were generated using the comb structure method [48]. In this method, a periodic array of line contacts is coupled to an ultrasonic transducer. The effect is to create a spatially periodic set of line sources on the plate surface, which results in an efficient source for generating Rayleigh or Lamb waves with a wavelength corresponding to the spatial periodicity of the contacts. For simplicity, the comb structure employed here was chosen to optimize the generation of a single Lamb wave mode, the fundamental antisymmetric mode A_0. To avoid excitation of higher order modes, the transducer was driven below the cutoff frequency of the next higher order (A_1) mode. This cutoff frequency can be determined from the relation $f_c = c_t/(2d)$, where d is the plate thickness and c_t is the bulk shear wave velocity for the plate material. Substituting values for an 1/8" (3.2 mm) aluminum plate with $c_t \approx 3.0$ mm/μs, f_c is estimated as 470 kHz. Here, the comb structure was driven by sinusoidal tone bursts of frequency 253 kHz, amplitude 0.7 V, and duration 133 ms. These input signals were amplified by an RF amplifier (ENI Model A150, nominal gain 55 dB) capable of delivering 150 W of continuous power into a 50-Ω load.

Influence of the lowest order symmetric mode, S_0 on the measurements was not significant for several reasons. First, the ESPI measurements are sensitive to out-of-plane displacements, which are primarily due to antisymmetric Lamb wave motion. Second, for the given plate thickness

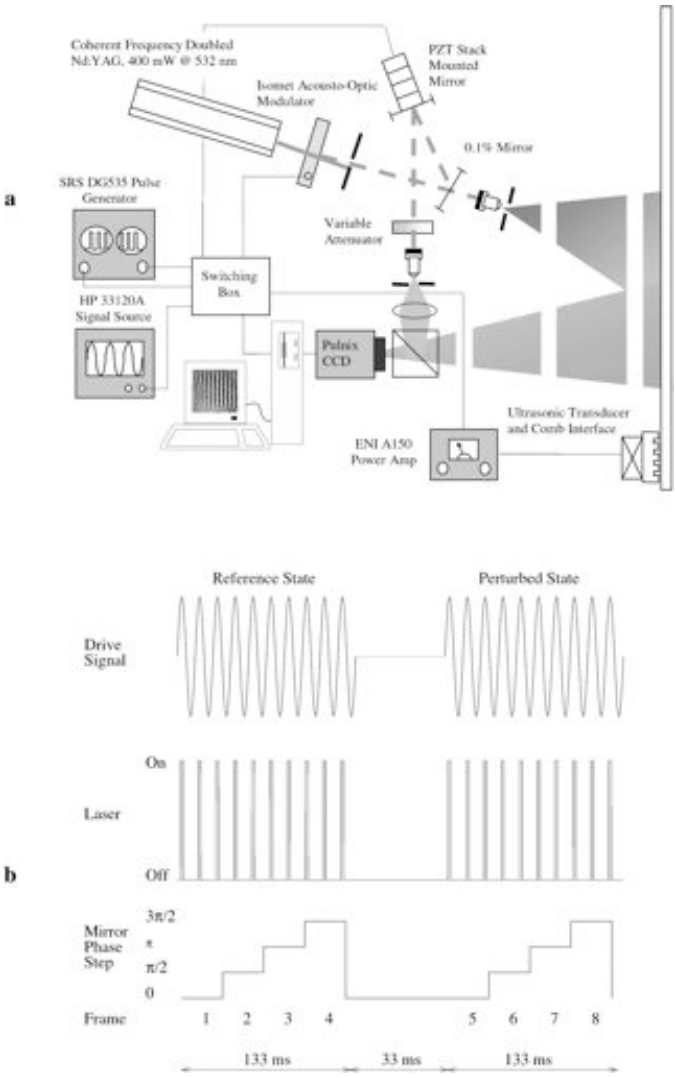

Fig. 5. Method for digital phase-stepping holography measurements. a) Sketch of the measurement apparatus; b) timing diagram illustrating control of the signal source, pulse generator, PZT stack, and acousto-optic modulator during data collection.

and operating frequency, the generation efficiency for the A_0 mode is approximately 35 dB larger than for the S_0 mode [49], assuming a point contact Hertzian load. In addition to this difference in generation efficiency for a point contact, the wavelength of the S_0 mode is greater than that of the A_0 mode by about a factor of three. Thus, the wavelength of the S_0 mode is significantly mismatched with the spatial periodicity of the comb structure, so that the generation efficiency of the S_0 mode is further inhibited relative to the A_0 mode.

Lamb waves were measured by the ESPI technique described previously for the 1/8" aluminum plate supported at two ends. Modeling clay was applied to all of the edges of the plate to absorb waves incident on the edges. Two flaws, a cross pattern of depth 2 mm and a circular hole of diameter 4.8 mm and depth 2 mm, were cut into the underside of the plate. These flaws are sketched in Fig. 6(a). A 1-3 composite source transducer was applied to the comb structure and driven at 253 kHz. The resulting surface wavefield is shown in Fig. 6(b). Although the defects can be observed to perturb the wavefield, their precise location, size, and shape are not easily determined by visual inspection of the ESPI data.

Quantitative reconstruction of the flaws was performed using the wavefield data of Fig. 6(b). The predominant background wavenumber k_0 was estimated using visual inspection of the spatial Fourier transform of the wavefield. The lowpass filter employed in the reconstruction formula of (10) was a Hanning window with radius $3\,k_0$, which was found to have less sensitivity to high frequency noise than the Blackman window employed in the simulations described previously. Otherwise, the reconstruction method was identical to that for the simulations. The resulting reconstruction, shown in Fig. 6(c), shows both the cross-shaped flaw and the small circular flaw much more clearly than the original ESPI data. An average of five independent reconstructions, each obtained from a separate 253-kHz wavefield measurement using the same transducer and ESPI configuration, is shown in Fig. 6(d). The averaging results in a substantial reduction of the optical noise and consequently shows the flaws more distinctly.

V. Discussion

The ESPI and image reconstruction methods described here could form part of a real-time structural inspection system. Because the present flaw imaging method can be directly implemented using FFT, quantitative flaw reconstruction could be added to present real-time ESPI systems (e.g., the shearography system described in [50]) without a significant increase in computational requirements. Flaw reconstructions could also be overlaid in real time onto optical images of the structure surface; this approach would allow inspectors to identify and characterize flaws while maintaining direct reference to the physical structure.

Reconstructions based on shearography wavefield measurements would differ from the present simulated and experimental results (based on TV holography measurements) in several minor ways. Electronic shearography is a common path interferometer that measures the differential displacements of the surface being monitored; TV holography directly measures the displacement of the surface. This distinction means that shearography does not require the levels of vibration isolation required for holography [29]–[32]. However, because shearography measures differential displacements between points separated by the "shearing distance", the optical amplitude is no longer directly proportional to the out-of-plane surface displacement. If the shearing distance is small compared with the Lamb wavelength, then the optical amplitude is proportional to the derivative of the surface displacement, and an appropriate

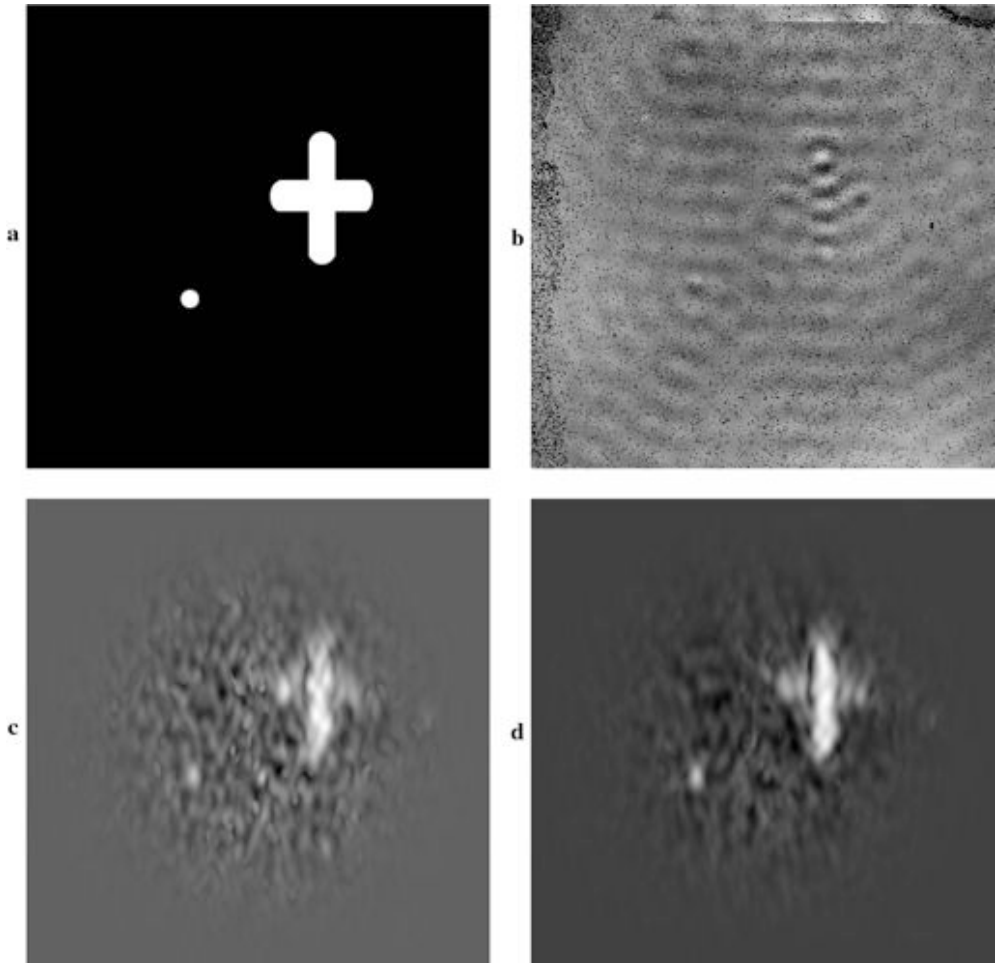

Fig. 6. Reconstruction of two flaws in an aluminum plate. Each panel shows an area of 13.6×13.6 cm^2. a) Sketch of the actual flaw positions, b) wavefield (253 kHZ) measured by digital phase stepping holography with waves incident from the top of the panel, c) flaw reconstruction from the measured wavefield shown in panel b, and d) average of flaw reconstructions from five independent optical wavefield measurements in the configuration of panel b.

inhomogeneous wave equation is obtained by taking the derivative of (2) along the shearing direction ξ,

$$\nabla^2 \frac{\partial u(x,y)}{\partial \xi} + k_0^2 \frac{\partial u(x,y)}{\partial \xi} = \frac{\partial Q(x,y)}{\partial \xi} + q(x,y)\frac{\partial u(x,y)}{\partial \xi} + u(x,y)\frac{\partial q(x,y)}{\partial \xi}. \quad (16)$$

Eq. (16) can be solved by the deconvolution methods described previously to determine the effective source terms that appear on the right-hand side. These effective source terms are directly related to the inhomogeneity function $q(x,y)$ of the structure examined, so that images constructed from shearography data using (16) would provide flaw maps similar to those shown here in Fig. 3, 4, and 6. However, the relationship between the effective sources of (16) and physical flaws is more complex than that of (2) and would be more difficult to interpret in terms of structural properties such as thickness and material composition.

ESPI measurements require a high optical signal-to-noise ratio, so that the present methods are most appropriate for high reflectivity surfaces. For structures with paint or coatings of low reflectivity, this problem can be overcome using thin layers of a temporary surface coating with high reflectivity, such as magnesium oxide powder [51]. In addition, the developer solution used in dye penetrant testing has been found to provide an effective temporary surface coating with high reflectivity.

Although the current imaging method is theoretically exact [for wavefields satisfying (2)], a number of factors place practical limits on the achievable image quality. Because the wavefield can, in practice, only be measured over a finite spatial region, the deconvolution method expressed by (10) is inherently approximate in practice. Still, the excellent delineation of the circular flaw boundary in all panels of Fig. 2 indicates that useful reconstructions can be obtained despite the approximations inherent to the method. The diffraction tomography reconstructions shown in Fig. 3 are of much lower quality, indicating that the approximations made by conventional inverse scattering methods are more severe than those of the present method.

The scattering formalism presented here, which employs a single free space Green's function, does not provide a

complete description of Lamb wave propagation and scattering in actual structures. Scattering and propagation of Lamb waves in inhomogeneous structures can involve mode conversion of elastic wave energy, including conversion into longitudinal waves. However, the present method could be adapted to employ multiple Green's functions associated with predominant modes of propagation, with wavenumbers either known a priori or determined from Fourier analysis of the ultrasonic wavefield. Because longitudinal bulk waves have significantly longer wavelengths than the low frequency A_0 modes, any mode-converted scattering should not contribute significantly to displacement images obtained using a wavenumber established a priori for the Lamb wave field. If no wavenumber is known a priori, the influence of mode-converted scattered waves could be minimized by measuring the effective wavenumber in wavefield regions where the incident Lamb wave mode contains most of the energy (e.g., in regions not including any strong scatterers).

Another possible concern is that the present method assumes strictly two-dimensional propagation; that is, the local particle displacement is assumed to be uniform throughout the plate thickness. This assumption is strictly valid only for plates that are very thin compared with the central acoustic wavelength λ_0. However, the experimental results shown previously suggest that the present imaging method is also applicable to thicker plates. That is, adequate flaw images were obtained even though the aluminum plate thickness was about $0.4\,\lambda_0$ for the ultrasonic frequency employed here.

The imaging method presented here has similar goals to those for the method presented in [52], in which inhomogeneities are reconstructed from multidimensional wavefields measured by a magnetic resonance imaging technique. The reconstruction algorithm used in [52] is an iterative, computationally intensive inverse scattering method based on a conjugate gradient descent procedure [15]. This iterative procedure results in accurate images of scatterers. However, because the reconstruction method employed in [52] can require many iterations for good reconstructions, that method is less well suited to real-time nondestructive testing than the direct deconvolution approach presented here.

Another related inverse scattering method is the nonlinear inverse scattering method of [16] and [43] in which sound-speed inhomogeneities are constructed using combinations of particular acoustic fields in the inhomogeneous medium. However, in that method, the acoustic fields are computed from estimates of the unknown medium; in the present method, the total wavefield is measured directly. The current method implicitly incorporates all effects associated with high contrast inhomogeneities, such as strong scattering and multiple scattering. This provides much more direct and accurate reconstructions than are possible from far-field scattering data.

The algorithm employed here for flaw reconstruction is formally more similar to methods of generalized holography, in which acoustic sources are imaged by measurement of the complex pressure along a surface in the acoustic near field. As in some implementations of generalized acoustic holography [39], [40], source distributions are determined here by deconvolution of a Green's function from a full wavefield. Both methods are theoretically exact and incorporate information from evanescent waves. One significant difference between the present reconstruction method and acoustic holography is that the present method images effective (scattering) sources rather than real sources. In addition, the current method employs wavefield measurements on the plane on which the real and effective sources exist, so that the step of numerical backpropagation, which is typically performed by the angular spectrum method in acoustic holography [39], [40] is not needed.

Because the current method employs deconvolution of image features from a multidimensional kernel, this method can also be compared with previous image enhancement methods employing deconvolution of image data (e.g., [53] and [54]). Such methods deconvolve a measurement-specific kernel, such as the point spread function of the transducer employed, to compensate for blurring caused by finite beam widths. Although the numerical methods employed here are similar, the basis for the present method is very different. Deconvolution is employed here as a fundamental image reconstruction method rather than an enhancement technique. Here, flaw images are created directly by deconvolving effective sources from the measured wavefield; in existing deconvolution methods [53], [54], images are first constructed by conventional (B-scan or C-scan) techniques and then enhanced by the deconvolution operation.

VI. Conclusions

A new method for nondestructive testing using ultrasonic wavefields measured by electronic speckle pattern interferometry has been presented. The method provides an efficient, direct means to obtain images of effective sources associated with scattering effects in plates and shells. A solution of the nonlinear inverse scattering problem via discrete Fourier transformation provides an imaging method suitable for real-time flaw imaging.

Results based on full wave simulated data show that high quality flaw reconstructions can be obtained from ideal data for a wide range of flaw contrast and size parameters. Successful imaging of flaw structures much smaller than the central wavelength indicates that evanescent wave information contributes to the reconstructions. Effective flaw reconstruction is also shown to occur even in the presence of large, high contrast, strongly scattering flaws. Comparison with diffraction tomography reconstructions indicates that the new ESPI-based imaging method provides accurate flaw images over a parameter range much wider than the usable range for conventional tomographic techniques.

Experimental results confirm that the present quantitative imaging method can effectively reconstruct flaws in plates. Flaw images obtained by this method give precise

indications of flaw locations, shapes, and sizes that are not possible to obtain from unprocessed ESPI wavefield measurements. These results suggest that the imaging method proposed here may be a useful tool for real-time nondestructive testing of plate and shell structures.

Acknowledgments

The authors thank Benjamin J. Bard for helpful discussions regarding digital phase-stepping shearography. Victor W. Sparrow is thanked for discussions regarding the radiation boundary condition of (15).

References

[1] C. Smith, "Federal Aviation Administration aircraft inspection research and development programs," *Proc. SPIE*, vol. 2945, pp. 200–209, 1997.

[2] S. I. Rokhlin, "Lamb wave interaction with lap-shear adhesive joints: Theory and experiment," *J. Acoust. Soc. Amer.*, vol. 89, no. 6, pp. 2758–2765, 1991.

[3] J. L. Rose, K. Rajana, and M.K.T. Hansch, "Ultrasonic guided waves for NDE of adhesively bonded structures," *J. Adhesion*, vol. 50, no. 1, pp. 51–82, 1995.

[4] A. Mal, Z. Chang, D. Guo, and M. Gorman, "Lap joint inspection using plate waves," *Proc. SPIE*, vol. 2945, pp. 128–137, 1997.

[5] J. D. Achenbach, "Detection and characterization of cracks and corrosion in aging aircraft structures (part II)," *Key Eng. Mater.*, vol. 145–149, pt. 2, pp. 1149–1160, 1998.

[6] J. L. Rose, A. Pilarski, K. Rajana, and J. J. Ditri, "Coating influence on generation and reception of ultrasonic Lamb type plate waves," in *Review of Progress in Quantitative Nondestructive Evaluation*. vol. 13, D. O. Thompson and D. A. Chimenti, Eds. New York: Plenum Press, 1994, pp. 1903–1910.

[7] G. A. Gordon and B. R. Tittmann, "Surface acoustic wave determination of subsurface structure," *Nondestr. Testing Eval.*, vol. 11, no. 1, pp. 21–32, 1994.

[8] W. P. Rogers, "Elastic property measurements using Rayleigh-Lamb waves," *Res. Nondestr. Eval.*, vol. 6, no. 4, pp. 185–208, 1995.

[9] G. A. Gordon and B. R. Tittmann, "Surface elastic wave measurement for determination of steel hardness gradients," in *Review of Progress in Quantitative Nondestructive Evaluation*. vol. 15, D. O. Thompson and D. A. Chimenti, Eds. New York: Plenum Press, 1996, pp. 1597–1604.

[10] Y. Hayashi, S. Ogawa, H. Cho, and M. Takemoto, "Non-contact estimation of thickness and elastic properties of metallic foils by the wavelet transform of laser-generated Lamb waves," *Nondestr. Testing Eval. Int.*, vol. 32, no. 1, pp. 21–27, 1999.

[11] D. P. Jansen and D. A. Hutchins, "Ultrasonic Rayleigh and Lamb wave tomography," *Acustica*, vol. 79, no. 2, pp. 117–127, 1993.

[12] Y. Nagata, J. Huang, J. D. Achenbach, and S. Krishnaswamy, "Lamb wave tomography using laser-based ultrasonics," in *Review of Progress in Quantitative Nondestructive Evaluation*. vol. 14, D. O. Thompson and D. A. Chimenti, Eds. New York: Plenum Press, 1995, pp. 561–568.

[13] W. Wright, D. Hutchins, D. Jansen, and D. Schindel, "Air-coupled Lamb wave tomography," *IEEE Trans. Ultrason., Ferroelect., Freq. Contr.*, vol. 44, pp. 53–59, 1997.

[14] J.C.P. McKeon and M. K. Hinders, "Lamb wave contact scanning tomography," in *Review of Progress in Quantitative Nondestructive Evaluation*. vol. 18A, D. O. Thompson and D. A. Chimenti, Eds. New York: Plenum Press, 1999, pp. 951–958.

[15] D. T. Borup, S. A. Johnson, W. W. Kim, and M. J. Berggren, "Nonperturbative diffraction tomography via Gauss-Newton iteration applied to the scattering integral equation," *Ultrason. Imag.*, vol. 14, no. 1, pp. 69–85, 1992.

[16] T. D. Mast, A. I. Nachman, and R. C. Waag, "Focusing and imaging using eigenfunctions of the scattering operator," *J. Acoust. Soc. Amer.*, vol. 102, no. 2, pp. 715–725, 1997.

[17] J.-P. Monchalin, "Optical detection of ultrasound," *IEEE Trans. Ultrason., Ferroelect., Freq. Contr.*, vol. 33, no. 5, pp. 485–499, 1986.

[18] C. B. Scruby and L. E. Drain, *Laser Ultrasonics: Techniques and Applications*. Bristol: Adam Hilger, 1990.

[19] A.D.W. McKie and R. C. Addison, "Practical considerations for the rapid inspection of composite materials using laser-based ultrasound," *Ultrasonics*, vol. 32, no. 5, pp. 333–345, 1994.

[20] P. W. Lorraine, "Laser ultrasound imaging of Lamb waves in thin plates," in *Review of Progress in Quantitative Nondestructive Evaluation*. vol. 17, D. O. Thompson and D. A. Chimenti, Eds. New York: Plenum Press, 1998, pp. 603–609.

[21] A. Blouin, D. Lévesque, C. Néron, F. Enguehard, D. Drolet, and J.-P. Monchalin, "SAFT data processing applied to laser-ultrasonic inspection," in *Review of Progress in Quantitative Nondestructive Evaluation*. vol. 17, D. O. Thompson and D. A. Chimenti, Eds. New York: Plenum Press, 1998, pp. 611–617.

[22] C. Wykes, "Advances in air-coupled ultrasonic transducers," *Nondestr. Test. Eval.*, vol. 12, no. 3, pp. 155–180, 1995.

[23] R. E. Green, "Emerging technologies for NDE of aging aircraft structures," in *Nondestructive Characterization of Aging Materials in Aging System*, Material Research Society Proc., vol. 503, R. L. Crane, J. D. Achenbach, S. P. Shah, T. E. Matikas, P. T. Khuri-Yakub, and R. A. Gilmore, Eds. Warrendale, PA: Materials Research Society, 1998, pp. 3–14.

[24] D. A. Hutchins, D. P. Jansen, and C. Edwards, "Lamb-wave tomography using non-contact transduction," *Ultrasonics*, vol. 31, no. 2, pp. 97–103, 1993.

[25] Z. Guo, J. D. Achenbach, and S. Krishnaswamy, "EMAT generation and laser detection of single Lamb wave modes," *Ultrasonics*, vol. 35, no. 6, pp. 423–429, 1997.

[26] J. Wagner, "Heterodyne holography for visualization of surface acoustic waves," *Nondestr. Testing Comm.*, vol. 2, no. 3, pp. 77–99, 1985.

[27] K.-J. Pohl, H.-A. Crostack, and H. Meyer, "Holographic visualization of laser generated ultrasound for the detection and description of sub-surface flaws," *Proc. SPIE*, vol. 1756, pp. 258–269, 1992.

[28] C. Henning and D. Mewes, "Visualization of surface waves propagating over surfaces eroded due to particle impact," *Wear*, vol. 186–187, no. 1, pp. 78–85, 1995.

[29] B. A. Bard, "Laser-modulated phase-stepping digital shearography for the quantitative analysis of structural vibration," Ph.D. dissertation, The Pennsylvania State University, 1997.

[30] B. A. Bard, G. A. Gordon, and S. Wu, "Laser-modulated phase-stepping digital shearography for quantitative full-field imaging of ultrasonic waves," *J. Acoust. Soc. Amer.*, vol. 103, no. 6, pp. 3327–3335, 1998.

[31] G. A. Gordon, B. A. Bard, and S. Wu, "Wide-area imaging of ultrasonic fields by digital phase-stepping shearography," in *Review of Progress in Quantitative Nondestructive Evaluation*. vol. 17, D. O. Thompson and D. A. Chimenti, Eds. New York: Plenum Press, 1998, pp. 1729–1736.

[32] J.-C. Krapez, F. Taillade, T. Lamarque, and D. Balageas, "Shearography: A tool for imaging Lamb waves in composites and their interaction with delaminations," *Review of Progress in Quantitative Nondestructive Evaluation*, vol. 18A, D. O. Thompson and D. A. Chimenti, Eds. New York: Plenum Press, 1999, pp. 905–912.

[33] H. Kolsky, *Stress Waves in Solids*. New York: Dover, 1963, ch. 3.

[34] P. M. Morse and K. U. Ingard, *Theoretical Acoustics*. New York: McGraw-Hill, 1968, ch. 8.

[35] P. M. Morse and H. Feshbach, *Methods of Theoretical Physics*. New York: McGraw-Hill, 1953, vol. I.

[36] I. N. Sneddon, *Fourier Transforms*. New York: McGraw-Hill, 1951.

[37] P. T. Christopher and K. J. Parker, "New approaches to the linear propagation of acoustic fields," *J. Acoust. Soc. Amer.*, vol. 90, no. 1, pp. 507–521, 1991.

[38] Z. G. Hah and K. M. Sung, "Effect of spatial sampling in the calculation of ultrasonic fields generated by piston radiators," *J. Acoust. Soc. Amer.*, vol. 92, no. 6, pp. 3403–3408, 1992.

[39] J. D. Maynard, E. G. Williams, and Y. Lee, "Nearfield acoustic holography: I. Theory of generalized holography and the development of NAH," *J. Acoust. Soc. Amer.*, vol. 78, no. 4, pp. 1395–1413, 1985.

[40] W. A. Veronesi and J. D. Maynard, "Nearfield acoustic holography: II. Holographic reconstruction algorithms and computer implementation," *J. Acoust. Soc. Amer.*, vol. 81, no. 5, pp. 1307–1322, 1987.
[41] E. Wolf, "Three-dimensional structure determination of semitransparent objects from holographic data," *Optics Comm.*, vol. 1, no. 4, pp. 153–156, 1969.
[42] A. J. Devaney, "A filtered backpropagation algorithm for diffraction tomography," *Ultrason. Imag.*, vol. 4, no. 4, pp. 336–350, 1982.
[43] T. D. Mast, A. I. Nachman, D.-L. Liu, and R. C. Waag, "Quantitative imaging with eigenfunctions of the scattering operator," in *Proc. IEEE Ultrason. Symp.*, pp. 1507–1510, 1997.
[44] V. W. Sparrow and R. Raspet, "A numerical method for general finite amplitude wave propagation and its application to spark pulses," *J. Acoust. Soc. Amer.*, vol. 90, no. 5, pp. 2683–2691, 1991.
[45] T. D. Mast, L. M. Hinkelman, M. J. Orr, V. W. Sparrow, and R. C. Waag, "Simulation of ultrasonic pulse propagation through the abdominal wall," *J. Acoust. Soc. Amer.*, vol. 102, no. 2, pp. 1177–1190, 1997.
[46] V. W. Sparrow and R. Raspet, "Absorbing boundary conditions for a spherical monopole in a set of two-dimensional acoustics equations," *J. Acoust. Soc. Amer.*, vol. 87, no. 6, pp. 2422–2427, 1990.
[47] G. A. Gordon and T. D. Mast, "Wide-area imaging of ultrasonic Lamb wave fields by electronic speckle pattern interferometry," *Proc. SPIE*, vol. 3586, pp. 297–309, 1999.
[48] I. A. Viktorov, *Rayleigh and Lamb Waves.* New York: Plenum Press, 1967.
[49] F. L. Degertekin and B. T. Khuri-Yakub, "Lamb wave excitation by Hertzian contacts with applications in NDE," *IEEE Trans. Ultrason., Ferroelect., Freq. Contr.*, no. 4, pp. 769–779, 1997.
[50] G. Lu, B. Bard, and S. Wu, "A real-time portable phase-stepping shearography system for NDE," *Proc. SPIE*, vol. 3397, pp. 156–167, 1998.
[51] R. Jones and C. Wykes, *Holographic and Speckle Interferometry.* 2nd ed. Cambridge: Cambridge University Press, 1989.
[52] V. Dutt, A. Manduca, R. Muthupillai, R. L. Ehman, and J. F. Greenleaf, "Inverse approach to elasticity reconstruction in shear wave imaging," in *Proc. IEEE Ultrason. Symp.*, pp. 1415–1418, 1997.
[53] S.-W. Cheng and M.-K. Chao, "Resolution improvement of ultrasonic C-scan images by deconvolution using the monostatic point-reflector spreading function (MPSF) of the transducer," *Nondestr. Testing Eval. Int.*, vol. 29, no. 5, pp. 293–300, 1996.
[54] X. Wang, C. J. Ritchie, and Y. Kim, "Elevation direction deconvolution in three-dimensional ultrasound imaging," *IEEE Trans. Med. Imag.*, vol. 15, no. 3, pp. 389–394, 1996.

T. Douglas Mast (M'98) was born in St. Louis, Missouri in 1965. He received a B.A. in physics and mathematics from Goshen College in 1987 and a Ph.D. in acoustics from The Pennsylvania State University in 1993. From 1993 until 1996, he was a postdoctoral research associate with the University of Rochester's Ultrasound Research Laboratory. Since 1996, he has been with the Applied Research Laboratory of The Pennsylvania State University, where he currently is a research associate and assistant professor of acoustics. His research interests include propagation and scattering in inhomogeneous media, inverse scattering, tissue characterization, and nondestructive testing.

Grant A. Gordon received his Bachelor of Science degree in engineering physics from Queen's University, Kingston, Ontario, in 1984. From 1985 to 1986, he worked as an optical systems engineer at Ernst Leitz Canada. He received the M.S. degree in 1990 and the Ph.D. in 1995, both from the Engineering Science and Mechanics program at The Pennsylvania State University. Until 1999, he was a research associate and assistant professor of acoustics at the Applied Research Laboratory of The Pennsylvania State University. Currently, he is Principal Engineer at McDermott Technology Inc. His research interests include guided elastic waves, nondestructive testing, material characterization, and noncontact ultrasonics.